Development of a Muscle Cell Engineering Platform Based on 3D Hydrogel Scaffolds for Functional Muscle Patch Production

Hyunmin Ryu

Received September 12, 2025
Accepted February 5, 2026
Electronic access March 15, 2026

Skeletal muscle injury leads to severe functional loss, and current treatments remain limited. In this study, we developed an innovative platform to engineer functional muscle patches by mimicking the natural microenvironment. We combined (i) a three-dimensional GelMA lattice scaffold to enhance nutrient diffusion and cell alignment and (ii) fibroblast-derived ECM priming to promote adhesion and differentiation. Under the combined ECM and 3D hydrogel lattice conditions, C2C12 attachment rates significantly increased, and long, parallel multinucleated myotubes formed along the lattice structure. Molecular analysis revealed strong upregulation of MyoD, Myogenin, and MRF4. Functionally, wound healing experiments demonstrated over 80% healing within 24 hours, and calcium imaging revealed synchronized contraction signals. This study presents an advanced in vitro muscle engineering platform that enhances myotube alignment and myogenic differentiation through the integration of a 3D hydrogel lattice scaffold and fibroblast-derived ECM priming. This system provides a foundation for future applications in implantable muscle patches and drug screening.

Keywords: 3D hydrogel lattice, ECM, 3T3, C2C12, muscle cell

Introduction

Skeletal muscle tissue performs functions essential for physical activity and metabolism[1,2], but, but it is easily damaged due to trauma, aging[3], and pathological conditions such as Duchenne Muscular Dystrophy (DMD)[4,5]. Such severe muscle damage often exceeds the tissue's spontaneous regenerative capacity[6], leading to functional loss[7]. Current treatments face limitations like transplant rejection and restricted functional recovery[8,9]. As an alternative to overcome these problems, research on muscle tissue reconstruction based on tissue engineering has been actively pursued[10,11]. . Conventional in vitro skeletal muscle models are predominantly based on two-dimensional (2D) planar cultures, which fail to recapitulate the three-dimensional architecture, mechanical constraints, and biochemical complexity of native muscle tissue[12]. In such environments, myoblast fusion and myotube alignment are often limited, resulting in structurally disorganized and functionally immature muscle constructs[13]. More recently, three-dimensional (3D) hydrogel-based culture systems have been introduced to overcome these limitations[14]. However, many bulk hydrogel models still suffer from insufficient structural guidance for cell alignment and limited integration of biochemical cues that are essential for muscle maturation[15]. As a result, although these models improve cellular encapsulation, they often fail to generate uniformly aligned and mature myotubes[16]. To address these limitations, there is a need for in vitro muscle models that integrate both physical and biochemical microenvironmental cues. Structural guidance that promotes anisotropic alignment, together with biologically relevant extracellular matrix (ECM) signals, is critical for driving efficient myoblast fusion and maturation[17]. However, platforms that effectively combine these elements in a reproducible and modular manner remain limited[18]. This study aims to construct a functional muscle patch by precisely mimicking the in vivo microenvironment of muscle tissue. To this end, we integrated two core strategies. First, we fabricated a 3D GelMA hydrogel scaffold with a lattice architecture to provides structural guidance that promotes myotube alignment and organization, while ECM priming enhances myogenic differentiation. Second, we applied fibroblast-derived extracellular matrix (ECM) priming to provide a biomimetic environment that assists in muscle cell attachment and maturation. This research goes beyond a simple in vitro model, presenting the potential of an innovative, implantable muscle patch and drug screening platform for muscle damage regeneration.

Literature Review

Skeletal Muscle Injury and Limitations of Current Regenerative Approaches

Despite the possibility of some limited intrinsic regeneration of skeletal muscle through satellite cells[19], in situations of extreme traumatic injury, degenerative ageing or associated with

some pathological conditions such as Duchenne muscular dystrophy (DMD), the regenerative capacity is nevertheless inadequate to replace the volumes of muscle that have been permanently compromised, leading to loss of function. Standard current approaches to skeletal muscle reconstruction including surgical reconstruction, autologous muscle grafts and stem-cell transplantations frequently result in poor prognosis in the clinic due to immune rejection, donor-site morbidity, poor engraftment efficiency and incomplete functional recovery[8].

The considerable limitations of skeletal muscle regeneration have led to increased interest in tissue engineered muscle constructs in regenerative medicine. Such constructs aim to replace the cellular component of muscles as well as their architecture and contractile properties. However, the generation of functional mature muscle tissue has been difficult due to the complexity of the muscle microenvironment and the challenges of recapitulating it in culture[20].

Limitations of Conventional 2D Muscle Cell Culture Models

Historically, most skeletal muscle studies have been performed in vitro using 2D planar cell culture systems. While these cultures are simple to set up and allow for repeatable experimental results, they fail to mimic the native physiological environment of the skeletal muscle due to their lack of structure and specific biochemical signals. Myoblasts in 2D cultures frequently display aberrant morphology, fusion deficiencies, poor alignment, and generate immature myotubes with sub-optimal cellular functions[21].

Prolonged culture in 2D will lead to partial myogenic differentiation; however, 2D culture systems produce myotubes that lack intrinsic fiber-type specification and maturity compared with muscle fibers in vivo[22]. In addition, 2D culture systems provide limited cell-cell and matrix-cell interactions[23]. Both of these extracellular interactions have been reported to be important in myogenic regulation[24]; therefore, there is a strong effort to develop 3D culture systems (i.e., culture systems that mimic in vivo muscle tissues) to study myogenesis.

Advances and Challenges in 3D Hydrogel-Based Muscle Tissue Engineering

Three-dimensional (3D) hydrogel scaffolds with tunable mechanical properties, high water content and biocompatibility have been tested in the field of skeletal muscle tissue engineering[25]. The hydrogels collagens, fibrin, alginates and gelatin methacryloyl (GelMA) have been utilized for encapsulation of myoblasts to foster their muscle tissue differentiation[16]. Of these, GelMA is particularly attractive as, besides containing the cell adhesive motif of gelatin, the stiffness and architecture can be easily manipulated by photopolymerization[26].

However, conventional bulk hydrogels suffer from some limitations: O_2 and nutrient diffusion is limited in dense hydrogels, resulting in low oxygen tension and low cell viability, especially in thicker constructs[27]. Furthermore, bulk hydrogels do not provide spatial cues for aligned myotubes, resulting in randomized orientation of muscle fibers and poor contractile function of the muscle construct[28]. To address this limitation, recent studies have incorporated structured or patterned hydrogels (microchannels, aligned fibers, or lattice structures) to promote diffusion and preferential cell orientation within the matrix[29].

Role of Extracellular Matrix in Myogenic Differentiation

Components of ECM (collagen, fibronectin, laminin etc.) are also involved in ECM-mediated signaling pathways that may define cell behavior by regulating myoblast adhesion, proliferation, and differentiation during development, regeneration, and maturation of skeletal muscle[30]. These factors are secreted by fibroblasts present in muscle tissue, which also represent the major cells responsible for the maintenance of the regenerative niche in skeletal muscle.

Previous reports have shown that fibroblast-synthesized ECM can initiate myogenic differentiation without MRF expression, indicating that cell matrix interactions are important determinants of myogenesis[31]. ECM proteins assist in focal adhesion assembly and cytoskeletal organization and may also exert their effects by modulating downstream signaling pathways that affect myotube fusion and maturation. However, many heterotypic in vitro muscle models use simplified or artificial ECM coatings that do not accurately recapitulate the complex composition of fibroblast-derived ECM[32]. Although ECM priming strategies that pre-coat hydrogels with endogenous ECM secreted by fibroblasts have been shown to improve myoblast attachment and differentiation[33], these strategies have mostly been adopted in 2D cultures and therefore may not accurately recapitulate the ECM architecture of the native 3D microenvironment of skeletal muscle.

Need for Integrated Structural and Biochemical Muscle Engineering Platforms

However, many of the most successful approaches to 3D muscle tissue engineering still rely on either mechanical or biochemical cues[34], with structured scaffolds maintaining the alignment of muscle cells, but lacking biochemical factors[35]. Likewise, ECM-based strategies enable improved differentiation but lack spatial organization[36]. Therefore, approaches that combine structural guidance and biologically relevant ECM signaling on platforms are still needed.

While engineered 3D structures and cell-derived ECM have been used as independent in vitro models, more recent works

suggest that the combination of both may better recapitulate the native muscle microenvironment and improve nutrient diffusion, cell alignment, myogenic differentiation, and functional maturation. However, the systematic evaluation of these combined strategies is limited[37].

Rationale for the Present Study

To overcome these limitations, we posit the use of a 3D GelMA lattice scaffold using fibroblast-derived ECM priming to develop a muscle tissue engineering platform. By utilizing a physically aligned, diffusive hydrogel lattice, combined with biologically active ECM components, the microenvironment of our muscle tissue engineering platform can better recapitulate the physiological conditions seen in vivo and thus can be applied to muscle development and regeneration. This allows the generation of fully functional and mature muscle patches for use in regenerative medicine and drug testing applications.

Materials and Methods

Preparation of 3D GelMA hydrogel lattice scaffold

Gelatin methacryloyl (GelMA, 10% (w/v)) was synthesized following standard protocols and dissolved in DPBS containing 0.05% (w/v) lithium phenyl-2,4,6-trimethylbenzoylphosphinate (LAP) as a photoinitiator. A GelMA concentration of 10% (w/v) was used throughout the study. This concentration was chosen to ensure sufficient mechanical integrity for stable lattice fabrication while maintaining a stiffness range reported to be permissive for myogenic differentiation[38].

Elastic molds were CAD-designed and fabricated using 3D printing (Formlabs, USA) with dimensions compatible with a 6-well plate. Each mold contained lattice patterns with a strut width of 1.0 mm, spacing of 2.0 mm, and thickness of 1.5 mm. GelMA solution was poured into the molds and photocrosslinked under UV light (405 nm, 10 mW/cm^2) for 30 s. The cured hydrogel lattices were carefully detached from the molds and stored in sterile DPBS until use.

To distinguish the effects of scaffold geometry from GelMA chemistry, flat GelMA and bulk GelMA controls were included. Flat GelMA substrates were prepared by casting a thin layer of GelMA on tissue culture plates followed by photocrosslinking. Bulk GelMA constructs were fabricated as non-patterned, continuous hydrogels using the same GelMA formulation and crosslinking conditions as the lattice scaffolds. All GelMA-based conditions shared identical polymer concentration and photoinitiator composition.

Cell culture and ECM priming

C2C12 murine myoblasts (ATCC, CRL-1772) and NIH3T3 fibroblasts (ATCC, CRL-1658) were cultured in Dulbecco's Modified Eagle Medium (DMEM, Gibco) supplemented with 10% fetal bovine serum (FBS, Gibco) and 1% penicillin/streptomycin at 37 °C with 5% CO_2. For ECM priming, NIH3T3 fibroblasts were seeded onto either 2D culture surfaces or 3D GelMA lattices and cultured for 5 days to allow deposition of ECM proteins (e.g., collagen I, fibronectin). To prevent fibroblast overgrowth, cells were treated with mitomycin-C (10 μg/mL, 2 h) prior to C2C12 seeding.

Myoblast seeding and differentiation

C2C12 myoblasts were seeded at a density of 1.0×10^4 cells per well (6-well) for flat controls or 5.0×10^3 cells per lattice scaffold. After 24 h in growth medium, cultures were switched to differentiation medium (DMEM supplemented with 2% horse serum) to induce myogenic differentiation. Medium was replaced daily for up to 4 days.

Electrical stimulation was applied at 1 Hz with a field strength of 5 V/cm and a pulse duration of 2 ms for 1 h per day. These parameters were selected based on previous reports showing that low-frequency electrical stimulation supports myogenic differentiation and calcium responsiveness while minimizing cellular stress and cytotoxic effects in C2C12 myotubes.

Immunofluorescence staining

Cells were fixed in 4% paraformaldehyde for 15 min, permeabilized with 0.1% Triton X-100, and blocked with 5% BSA. Samples were incubated overnight with primary antibodies against Myosin Heavy Chain (MHC, MF20, DSHB, 1:200) and α-actinin (Sigma, 1:200), followed by Alexa Fluor-conjugated secondary antibodies (Invitrogen, 1:500). Nuclei were counterstained with DAPI (1 μg/mL). Images were acquired using a confocal microscope (Zeiss LSM800) and analyzed with ImageJ. Fusion Index (FI, % of nuclei within MHC$^+$ myotubes with ≥ 2 nuclei/total nuclei) and Orientation Order Parameter (OOP, 0–1 scale) were quantified from ≥ 5 random fields.

Gene expression analysis (RT-qPCR)

Total RNA was extracted using TRIzol (Invitrogen), and cDNA was synthesized using a reverse transcription kit (Thermo Scientific). Quantitative PCR was performed using SYBR Green Master Mix (Bio-Rad) with primers specific for MyoD, Myogenin, MRF4, and GAPDH as an internal control. Relative expression was calculated using the $\Delta\Delta Ct$ method.

Table 1: Primer sequences of RT-qPCR

	Forward (5′–3′)	Reverse (5′–3′)
MyoD	GATGCACCGGTTATTTGGGG	ATTCCCTGTAGCACCACACA
Myogenin	AAGAAGGGGAGAGGAACAGC	GCAACTTCAGCACAGGAGAC
MRF4 (Myf6)	GTGGAGGAAGTGGTGGAGAA	GCATGCACAACAGATTTCGC

Western blotting

Proteins were extracted with RIPA buffer containing protease inhibitors, separated by SDS-PAGE, and transferred to PVDF membranes. Membranes were blocked with 5% skim milk and probed with primary antibodies against MyoD(Santa Cruz; sc-32758), Myogenin(Santa Cruz; sc-12732), MRF4(Invitrogen; PA5-97990), and β-actin (Santa Cruz; sc-8432). HRP-conjugated secondary antibodies were used, and bands were visualized by ECL detection (Bio-Rad). Densitometry analysis was performed using ImageJ.

Wound healing assay

A scratch wound was generated using a sterile 200 μL pipette tip across confluent C2C12 cultures (flat, 2D ECM primed, 3D lattice ECM primed). Images were captured at 0 h and 24 h, and wound area was quantified using ImageJ. Relative wound closure (%) was calculated as:

$$\text{Wound closure}(\%) = \frac{A_{0h} - A_{24h}}{A_{0h}} \times 100$$

Calcium imaging

Calcium imaging was performed to compare relative calcium signal intensity across myotubes under different culture conditions. Cells were loaded with Fluo-4 AM, and fluorescence images were acquired at a single time point during electrical stimulation. Mean fluorescence intensity was quantified using ImageJ to assess calcium responsiveness.

Non-stimulated control samples were prepared for each condition. However, in the absence of electrical stimulation, calcium fluorescence signals remained near baseline levels and were close to the detection limit. Therefore, quantitative comparisons of calcium responses were performed under electrically stimulated conditions.

Statistical analysis

All experiments were independently repeated at least three times. For all quantitative analyses, n denotes the number of independent biological replicates. Data are presented as mean $\pm$ standard deviation (SD). Statistical significance was determined using one-way ANOVA followed by Tukey's post hoc test. A value of $p < 0.05$ was considered significant.

All statistical summary tables used in this study are provided in the Supplementary Data.

Results

Fabrication and Characterization of 3D GelMA Hydrogel Lattice Scaffolds

A CAD-designed elastic mold was 3D printed, and a release coating was applied to its surface to facilitate easy demolding of the GelMA (Figure 1a and 1b). The fabricated scaffolds maintained excellent mechanical stability, making them suitable for long-term cell culture.

ECM Priming and Initial Cell Attachment

To precisely mimic the in vivo muscle microenvironment, we performed fibroblast-derived extracellular matrix (ECM) priming. This is because fibroblasts secrete various ECM proteins, such as collagen and fibronectin, which are important for muscle tissue maturation and maintenance. These ECM proteins not only act as a physical support for cell attachment and spreading but also serve as catalysts that provide biochemical signals influencing cell differentiation.

We divided the experiment into three conditions to investigate the ECM priming capability of fibroblasts and the efficacy of our fabricated 3D hydrogel lattice scaffold (Figure 2a and 2b). The first condition was seeding only myoblasts (C2C12) without ECM priming. The second condition was inducing fibroblasts (3T3) to naturally secrete ECM by seeding them in a 2D environment for 5 days before seeding C2C12. The third condition was culturing 3T3 cells first on the 3D hydrogel lattice we made to prime the ECM, and then seeding C2C12. After culturing 3T3 for ECM priming, we treated the cells with mitomycin-c to inhibit 3T3 proliferation, preventing complex growth competition between muscle cells and fibroblasts and creating a pure ECM environment.

The initial cell attachment rate of C2C12 cells in ECM-primed Case 2 was about 1.4 times higher than in Case 1 (Flat), and it increased to 1.7 times in Case 3 (Figure 2c). This

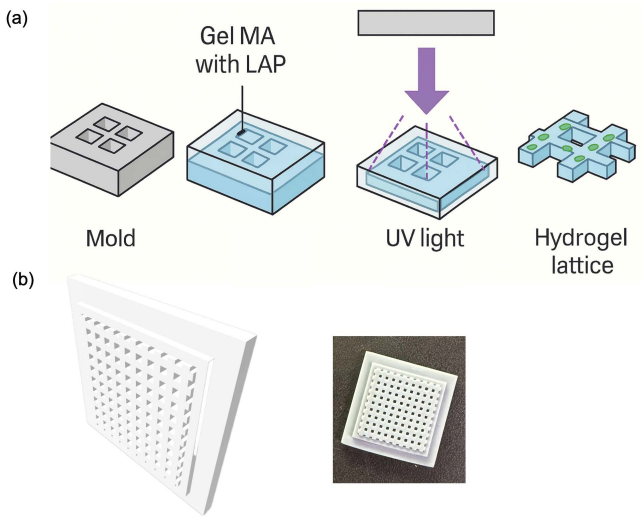

Fig. 1: .a) Schematic illustration of the fabrication process. A 3D-printed elastic mold was prepared and filled with GelMA solution (10%) containing LAP (0.05%) as a photoinitiator. Upon UV irradiation (405 nm), the solution was photocrosslinked and detached from the mold, yielding a mechanically stable hydrogel lattice scaffold. (b) CAD-based design and the product of the mold compatible with a 6-well plate, enabling reproducible fabrication of lattice structures with uniform thickness (1.5 mm), strut width (1.0 mm), and spacing (2.0 mm). The resulting hydrogel lattice provides a 3D environment that facilitates nutrient diffusion and guides cellular alignment.

proves that the ECM secreted by fibroblasts successfully provided an environment favorable for the attachment and survival of myoblasts.

Muscle Cell Differentiation and Molecular Characterization

To verify muscle cell differentiation at the morphological and molecular levels, we performed immunofluorescence staining, RT-qPCR, and Western blot analysis. First, MHC immunofluorescence staining results showed that most single-nucleus cells were observed in Case 1, and the formed myotubes were short and arranged in an irregular direction. In contrast, in the 2D condition with ECM priming (Case 2), multinucleated myotubes were distinctly increased, and cell-to-cell connections were strengthened, leading to a significant improvement in the length and thickness of myotubes compared to the Flat condition. Particularly, the most prominent results were observed in the condition where ECM priming was applied on the 3D lattice (Case 3). In Case 3, myotubes grew the longest, and a clear structure of parallel alignment along the direction of the lattice was observed (Figure 3).

Along with morphological analysis, RT-qPCR confirmed the expression of muscle differentiation-related transcription factors. In the ECM-primed Case 2, the expression of MyoD, Myogenin, and MRF4 increased by approximately 1.4, 1.51, and 1.63 times, respectively, compared to the Flat condition. In Case 3, which combined the 3D lattice and ECM priming, the expression of these genes increased even more significantly, with MyoD, Myogenin, and MRF4 rising by up to 1.87, 2.69, and 2.35 times, respectively (Figure 3) ($n = 3$ independent experiments; one-way ANOVA followed by Tukey's post hoc test). These results suggest that when ECM and 3D structures are combined, muscle cell differentiation and maturation signals are strongly induced.

Furthermore, Western blot analysis confirmed a similar trend at the protein level. The expression of MyoD, Myogenin, and MRF4 proteins showed an increasing tendency from Case 1 to Case 3 (Figure 3). Among the GelMA-based conditions, lattice-structured scaffolds consistently exhibited higher expression of MyoD, Myogenin, and MRF4 compared to flat and bulk GelMA controls (Figure 3).This supported the finding that muscle cell fusion and maturation were greatly enhanced in the ECM-primed and lattice scaffold environment.

Verification of Regenerative and Functional Properties of the Muscle Patch

To evaluate cell migratory behavior, a scratch wound assay was performed under each experimental condition. In the Flat condition, the damage area induced by the scratch remained over 70% even after 24 hours, and the recovery speed was relatively slow. In contrast, the damage recovery speed in Case 2 increased by 26.5% compared to Case 1. Notably, the fastest

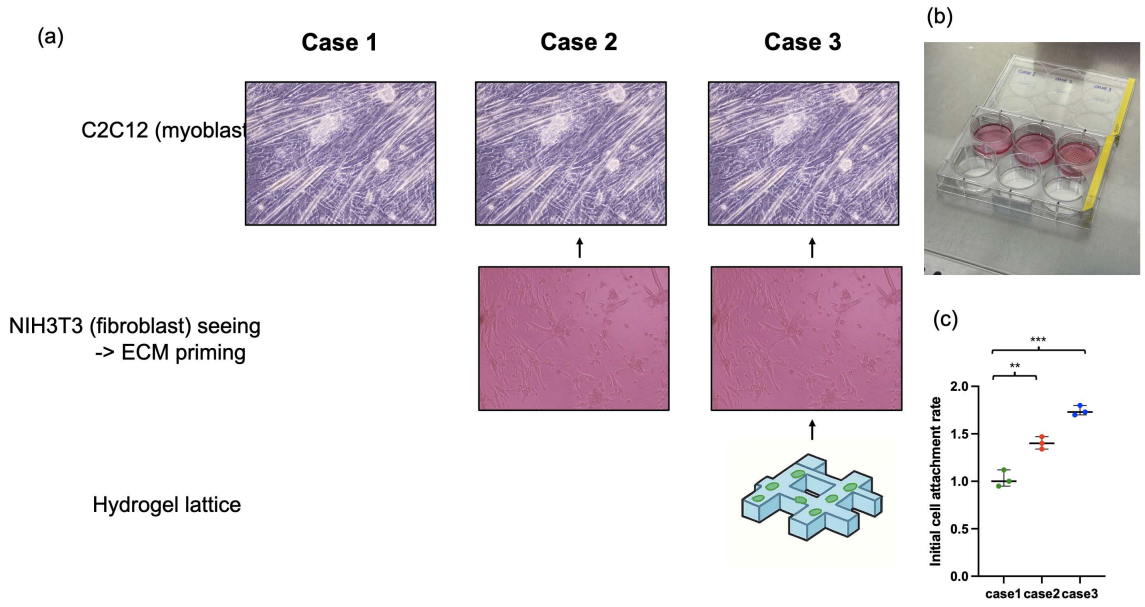

Fig. 2: Comparison of myotube morphology across GelMA-based culture conditions. (a,b) Representative images showing differences in myotube organization and alignment on flat GelMA, bulk GelMA, and lattice-structured GelMA scaffolds. (c) Quantitative analysis of myotube alignment derived from morphological measurements. Data are presented as mean ± SD ($n \geq 3$).

healing ability, exceeding 80%, was observed in Case 3 (Figure 4). These results are associated with fibroblast-derived ECM priming and indicate enhanced myotube morphology and myogenic gene expression under these conditions.

Additionally, to verify that the patch not only has regenerative ability but also possesses functional properties similar to actual muscle, we performed Calcium Imaging. Calcium fluorescence intensity was quantified at a single time point during electrical stimulation to compare relative calcium responsiveness across conditions. Particularly, the lattice+ECM group showed a signal accompanied by strong contractile twitch (Figure 4), proving that it mimics the electrophysiological properties of muscle tissue.

Discussion

This study successfully demonstrated the potential for developing a functional muscle patch by combining a 3D hydrogel lattice scaffold with fibroblast-derived extracellular matrix (ECM) priming as a new therapeutic strategy for muscle damage. The attempt to precisely mimic the structural and biochemical microenvironment of actual muscle tissue, overcoming the limitations of conventional 2D planar culture and simple bulk 3D models, led to very meaningful results.

The lattice-structured GelMA scaffold we fabricated provided an optimal physical environment for muscle cell survival and differentiation. Unlike simple bulk hydrogels, the lattice structure offered a large surface area, enabling efficient diffusion of oxygen and nutrients[39,40]. Furthermore, the regular struts and spacing of the scaffold guided cells to align naturally along their direction. As shown by the immunofluorescence staining results, this played a crucial role in the formation of long, parallelly aligned multinucleated myotubes. Such structural alignment is an essential factor for restoring the functional properties, such as contractility, of muscle tissue.

Fibroblast-derived ECM priming played a core role in creating a biomimetic environment necessary for muscle cell differentiation and maturation[31,41]. Various ECM proteins (collagen, fibronectin, etc.) secreted by fibroblasts significantly increased the initial attachment and survival rates of myoblasts[42]. This reconfirmed that the interaction between cells and the matrix is a crucial signal that determines the cell's fate[43,44]. In particular, the significant increase in the expression of muscle differentiation-related genes (MyoD, Myogenin, MRF4) in RT-qPCR and Western blot analysis suggests that ECM signals strongly promote the cell's differentiation pathway.

Furthermore, among the tested conditions, the lattice-guided and ECM-primed constructs (case 3) consistently showed higher myogenic marker expression. The physical lattice structure provided the 'direction' for cell alignment,

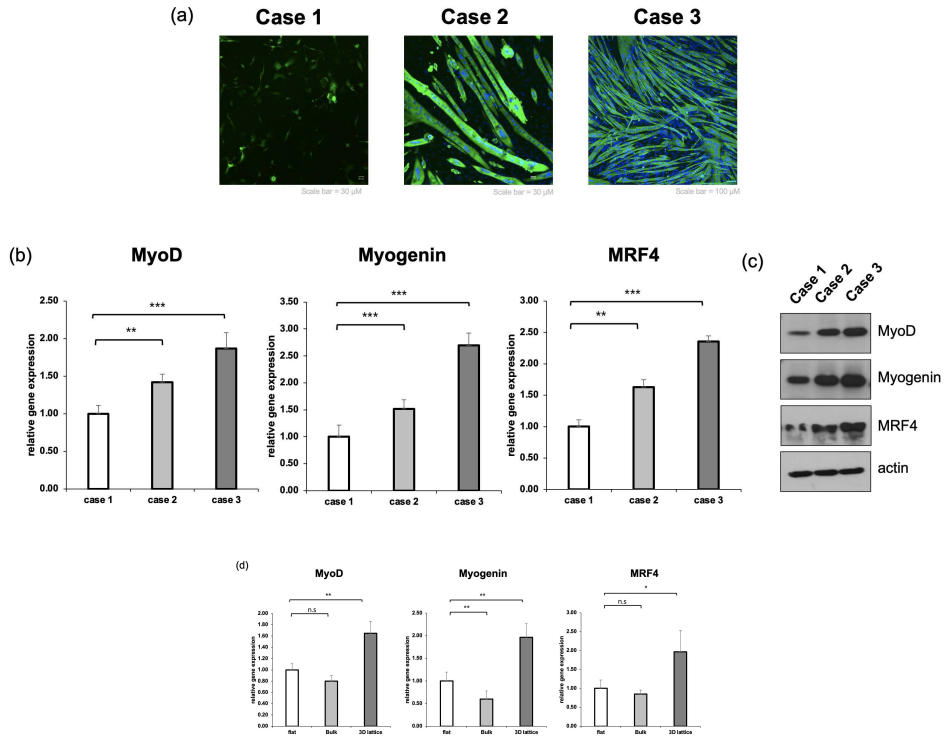

Fig. 3: (a) Immunofluorescence staining of Myosin Heavy Chain (MHC, green) and nuclei (DAPI, blue) in Case 1 (flat C2C12 only), Case 2 (2D ECM priming + C2C12), and Case 3 (3D lattice + ECM priming + C2C12). Case 3 exhibited the longest and most aligned multinucleated myotubes compared to Case 1 and Case 2. (b) Relative mRNA expression of myogenic markers MyoD, Myogenin, and MRF4 as determined by RT-qPCR. Data are shown as mean $\pm$ SD; $n = 3$, $^{**}p < 0.01$, $^{***}p < 0.001$. (c) Western blot analysis of MyoD, Myogenin, and MRF4 protein expression. Actin was used as a loading control. (d) Relative mRNA expression of myogenic markers MyoD, Myogenin, and MRF4 as determined by RT-qPCR. Data are shown as mean $\pm$ SD; $n = 3$, n.s.=non-significant, $^{*}p < 0.05$, $^{**}p < 0.01$.

while the biochemical ECM signals promoted the 'speed' and 'intensity' of cell differentiation, thereby constructing an optimized environment for muscle tissue reconstruction. This was clearly demonstrated in the wound healing assay and calcium imaging results. The Case 3 group showed the fastest wound recovery speed and synchronized calcium signals, suggesting that it can secure functional viability similar to actual muscle tissue, going beyond mere cell survival. However, it should be noted that the scratch assay primarily reflects cell migration and proliferation in an in vitro setting and does not represent true skeletal muscle regeneration. Therefore, the observed wound closure is interpreted as enhanced migratory behavior rather than tissue repair. Also, it should be noted that calcium imaging was performed at a single time point, which does not allow direct assessment of synchronous contraction or excitation–contraction coupling dynamics. In addition, measurements of contractile force, twitch kinetics, or time-resolved calcium transients were not included in this study. These functional assessments will be essential in future work to further validate muscle-like behavior of the engineered constructs.

The 3D lattice hydrogel scaffold-based muscle tissue engineering platform developed in this study presents an innovative method for the successful in vitro reconstruction of muscle tissue. Although the engineered constructs exhibited improved myotube alignment and increased expression of myogenic markers, this study does not demonstrate the formation of a mechanically integrated, force-generating muscle tissue. Together, these findings suggest that the lattice-structured GelMA scaffold, in combination with fibroblast-derived ECM priming, provides a microenvironment that supports myoblast organization and differentiation in vitro. However, the present data do not demonstrate the formation of a fully functional, force-generating muscle tissue. Nevertheless, this platform can be utilized in the future as a drug screening model for diseases like muscular dystrophy.

Future studies should focus on further in vitro validation of functional properties, including measurements of contractile

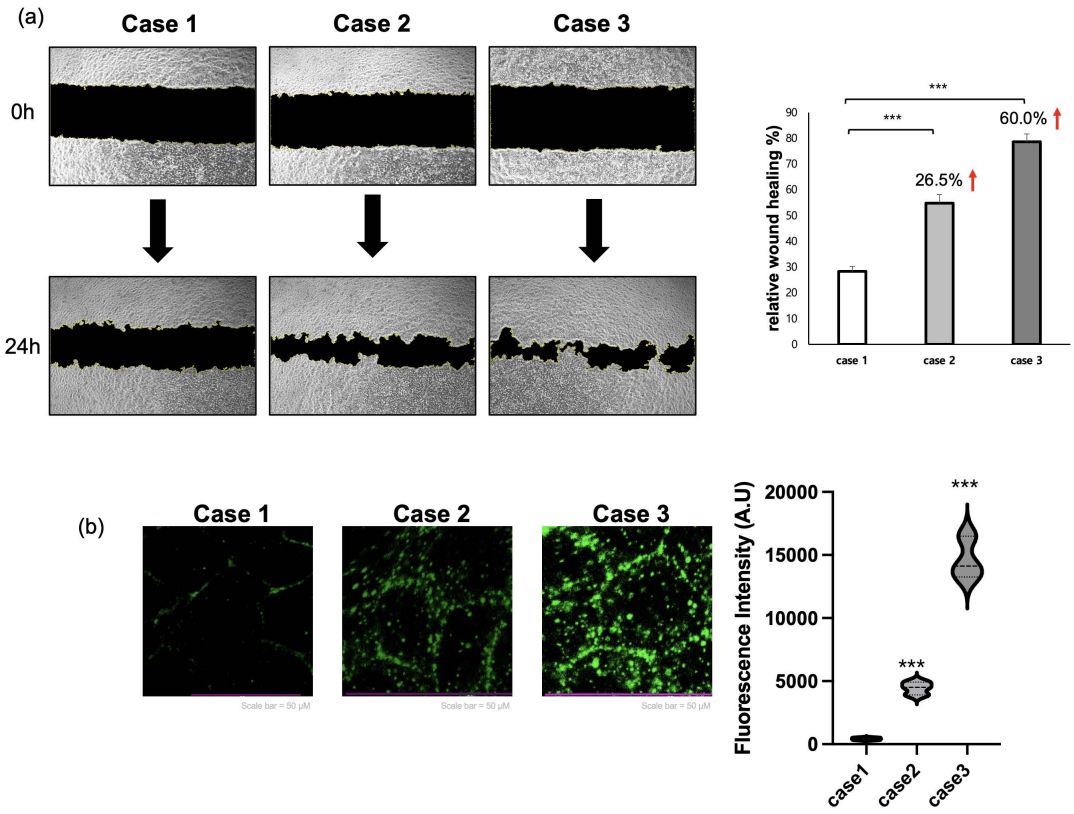

Fig. 4: (a) Representative images of scratch wound closure in Case 1, Case 2, and Case 3. Yellow outlines indicate wound boundaries at 0 h and 24 h (Left). Quantitative analysis of relative wound healing rate. Case 1 achieved $\sim 28\%$ closure, Case 2 improved to $\sim 55\%$ (26.5% increase), and Case 3 reached $\sim 81\%$ closure (60.0% increase) within 24 h. Data are presented as mean $\pm$ SD; $n = 3$; $^{***}p < 0.001$. (b) Fluorescence intensity was captured at a single time point to compare calcium levels across different myotubes. Representative images (top) and violin plot (bottom) show relative calcium signal intensity, reflecting synchronous activity and functional status of the myotubes under each experimental condition. $n = 3$, $^{***}p < 0.001$.

force, time-resolved calcium transients, and refined electrical stimulation protocols. These steps will be essential to better characterize muscle-like behavior before considering more advanced applications. In summary, this study presents an advanced in vitro platform for investigating how structural and biochemical cues influence myogenic differentiation, while highlighting the need for additional functional validation in future work.

References

1 B. Egan and J. R. Zierath, *Cell Metabolism*, 2013, **17**, 162–184.
2 M. C. K. Severinsen and B. K. Pedersen, *Endocrine Reviews*, 2020, **41**, 594–609.
3 D. T. Kirkendall and W. E. Garrett, *The American Journal of Sports Medicine*, 1998, **26**, 598–602.
4 C. Godi *et al.*, *Annals of Clinical and Translational Neurology*, 2016, **3**, 607–622.
5 B. De Paepe and J. L. De Bleecker, *Mediators of Inflammation*, 2013, **2013**, 540370.
6 B. T. Corona, C. L. Ward, H. B. Baker, T. J. Walters and G. J. Christ, *Tissue Engineering Part A*, 2014, **20**, 705–715.
7 H. Kern *et al.*, *Neurorehabilitation and Neural Repair*, 2010, **24**, 709–721.
8 S. M. Maffioletti, M. Noviello, K. English and F. S. Tedesco, *BioMed Research International*, 2014, **2014**, 964010.
9 S. M. Greising, C. L. Dearth and B. T. Corona, *Cells Tissues Organs*, 2016, **202**, 237–249.
10 M. Samandari *et al.*, *Advanced Materials*, 2022, **34**, 2105883.
11 J. Gilbert-Honick and W. Grayson, *Advanced Healthcare Materials*, 2020, **9**, 1900626.
12 Y. Gao *et al.*, *Regenerative Biomaterials*, 2025, **12**, 1–10.
13 M. Afshar Bakooshli *et al.*, *eLife*, 2019, **8**, e44530.
14 A. S. T. Smith, S. Passey, L. Greensmith, V. Mudera and M. P. Lewis, *Journal of Cellular Biochemistry*, 2012, **113**, 1044–1053.
15 A. S. Salimath and A. J. García, *Journal of Tissue Engineering and Regenerative Medicine*, 2016, **10**, 967–976.
16 M. Costantini *et al.*, *Frontiers in Bioengineering and Biotechnology*, 2017, **5**, 10588–10612.

17 S. Jana, S. K. L. Levengood and M. Zhang, *Advanced Materials*, 2016, **28**, 10588–10612.
18 R. Raman, C. Cvetkovic and R. Bashir, *Nature Protocols*, 2017, **12**, 519–533.
19 N. Motohashi and A. Asakura, *Frontiers in Cell and Developmental Biology*, 2014, **2**, e44530.
20 Y. Jin *et al.*, *Advanced Materials*, 2021, **33**, 2007946.
21 P.-Y. Wang, H.-T. Yu and W.-B. Tsai, *Biotechnology and Bioengineering*, 2010, **106**, 285–294.
22 S. T. Cooper *et al.*, *Cell Motility*, 2004, **58**, 200–211.
23 O. Habanjar *et al.*, *International Journal of Molecular Sciences*, 2021, **22**, 12200.
24 U. Mayer, *Journal of Biological Chemistry*, 2003, **278**, 14587–14590.
25 L. Wang, Y. Wu, B. Guo and P. X. Ma, *ACS Nano*, 2015, **9**, 9167–9179.
26 P. Chansoria *et al.*, *ACS Biomaterials Science & Engineering*, 2021, **7**, 5175–5188.
27 L. Figueiredo *et al.*, *Journal of Tissue Engineering and Regenerative Medicine*, 2018, **12**, 1238–1246.
28 K. J. De France *et al.*, *Nano Letters*, 2017, **17**, 6487–6495.
29 S. Sornkamnerd, M. K. Okajima, K. Matsumura and T. Kaneko, *ACS Applied Materials & Interfaces*, 2018, **10**, 44834–44843.
30 D. Docheva, C. Popov, P. Alberton and A. Aszodi, *Birth Defects Research Part C*, 2014, **102**, 13–36.
31 N. Osses and E. Brandan, *American Journal of Physiology-Cell Physiology*, 2002, **282**, C383–C394.
32 T. Cao and C. R. Warren, *Cells*, 2025, **14**, 882.
33 M. Boyd-Moss *et al.*, *Advanced NanoBiomed Research*, 2022, **2**, 2100106.
34 B. Bakhshandeh *et al.*, *Bioengineering & Translational Medicine*, 2023, **8**, e10383.
35 G. C. Bandara, R. D. Boudreau, W. Wyatt and S. R. Caliari, *bioRxiv*, 2025.
36 S. Nakada, *Unspecified journal*, 2024.
37 A. Sala *et al.*, *Integrative Biology*, 2011, **3**, 1102–1111.
38 C. Peyret *et al.*, *International Journal of Molecular Sciences*, 2023, **24**, 123–130.
39 E. Axpe *et al.*, *Macromolecules*, 2019, **52**, 6889–6897.
40 F. V. Lavrentev *et al.*, *Molecules*, 2023, **28**, 5931.
41 F. Melo, D. J. Carey and E. Brandan, *Journal of Cellular Biochemistry*, 1996, **62**, 227–239.
42 A. Uchinaka *et al.*, *European Journal of Cardio-Thoracic Surgery*, 2016, **51**, 457–464.
43 Y. Bi *et al.*, *Journal of Biological Chemistry*, 2005, **280**, 30481–30489.
44 E. Chermnykh, E. Kalabusheva and E. Vorotelyak, *International Journal of Molecular Sciences*, 2018, **19**, 1003.

Supplementary Tables

Table 2: Summary of quantitative results of figure 2c

	case 1	case 2	case 3
initial cell attachment rate	1	1.4	1.7
	1.12	1.47	1.8
	0.95	1.34	1.73

Table 3: Summary of quantitative results of figure 3b.

	Myo D relative expression			Myogenin relative expression			Mrf4 relative expression		
Expression	Case 1	Case 2	Case 3	Case 1	Case 2	Case 3	Case 1	Case 2	Case 3
Average	1	1.42	1.8667	1	1.5133	2.6933	1.0033	1.63	2.3533
SD	0.11	0.1082	0.2123	0.213	0.17	0.23	0.1050	0.1179	0.089

Table 4: Summary of quantitative results of figure 3d

	Mrf4 relative expression								
expression	flat			bulk			3d lattice		
	flat	bulk	3d lattice	flat	bulk	3d lattice	flat	bulk	3d lattice
average	1	0.8	1.65	1	0.6	1.966666667	1.00333333	0.85	1.966666667
SD	0.11	0.1	0.2322	0.197	0.18	0.305505046	0.221	0.11	0.56862407

Table 5: Summary of quantitative results of figure 4a

	case 1	case 2	case 3
relative wound healing (%)	26.217677	57.68087539	75.27458319
	28.435	51.234	79.13
	30.123	55.4	81.2
average	28.258559	54.77162513	78.53486106
SD	1.958631029	3.269050596	3.007205323

Table 6: Summary of quantitative results of Figure 4b

	Case 1	Case 2	Case 3
Fluorescence intensity 1 (A.U.)	326	4919	16500
Fluorescence intensity 2 (A.U.)	424	3913	13255
Fluorescence intensity 3 (A.U.)	519	4500	14119
Average	423	4444	14624.67
SD	96.50	505.33	1680.56